

Virtual Coil Augmentation Technology for MRI via Deep Learning

Cailian Yang, Xianghao Liao, Yuhao Wang, Minghui Zhang, Qiegen Liu

Abstract—Magnetic resonance imaging (MRI) is a widely used medical imaging modality. However, due to the limitations in hardware, scan time, and throughput, it is often clinically challenging to obtain high-quality MR images. In this article, we propose a method of using artificial intelligence to expand the channel to achieve the effect of increasing the virtual coil. The main feature of our work is utilizing dummy variable technology to expand the channel in both the image and k-space domains. The high-dimensional information formed by channel expansion is used as the prior information of parallel imaging to improve the reconstruction effect of parallel imaging. Two features are introduced, namely variable enhancement and sum of squares (SOS) objective function. Variable argumentation provides the network with more high-dimensional prior information, which is helpful for the network to extract the deep feature information of the image. The SOS objective function is employed to solve the problem that k-space data is difficult to train while speeding up the convergence speed. Ablation studies and experimental results demonstrate that our method achieves significantly higher image reconstruction performance than current state-of-the-art techniques.

Keywords—Virtual coil, Reversible network, Variable argumentation, Parallel imaging, Super-resolution.

I. INTRODUCTION

From the development of the magnetic resonance imaging (MRI) phased array [1] until recently, most MRI scanners employed a modest number of receiver coils, used primarily to enhance the signal-to-noise ratio (SNR) over relatively large fields of view (FOV). The simultaneous use of multiple receiver coils was pioneered in the late 1980s [2-4] and analyzed in detail by Roemer et al. [5]. However, driven in large part by the advent of parallel imaging [6-10], the number of MRI receive coils have recently blossomed. A number of groups have reported results for 32 coils [6] or 64 coils [7], with recent conference have reported presenting preliminary work on 90 coils [8], 96 coils [9], and 128 coils [10], [11]. The simultaneous use of a large number of receiver coils in principle enables high reduction factors for parallel imaging and improves SNR near the surface.

Due to the obvious benefits of large coil arrays for SNR and acceleration, both researchers and manufacturers have been developing and building large dedicated arrays [12]-[15]. However, packing receiver-coil electronics into a small region can compound coil coupling and losses, affect flexi-

bility and weight. Additionally, it results in increased memory usage and large computational costs for reconstructing the missing data from such a large number of coils. In this study, we will use channel expansion technology in parallel imaging to promote resolution enhancement and fast reconstruction. For further description, we will introduce super-resolution (SR) and parallel imaging (PI) algorithms, respectively.

A. Review of SR

Roughly speaking, SR algorithms can be divided into two categories: Model-based and learning-based. Interpolation algorithms [16]-[18], like bilinear, bicubic, and nearest-neighbor interpolation techniques, are representatives of simple model-based approaches, which can be directly used to enlarge images. Wiener filtering and iterative deblurring algorithms utilize knowledge on the system point spread function to recover image resolution [19], [20] and are also considered as model-based algorithms. Dictionary learning-based SR techniques [21]-[22] are examples of learning-based algorithms. The performance of these conventional methods is essentially limited because they apply inadequate additional information and models with limited representational capacity to solve the notoriously challenging ill-posed inverse problem of image SR tasks.

Over the past decades, deep learning methods have expanded the learning-based SR methods and gained increasing attention. Especially, convolutional neural networks (CNN) based models have become one kind of the most popular methods in MRI SR, because of their simple network structure and high restoration accuracy. As a pioneer work, Dong et al. [23] first proposed the convolutional CNN-based SR (SRCNN) algorithm, which directly learned an end-to-end mapping from LR images to HR images. After the SRCNN outperformed other learning-based SR algorithms [23], [24], various deep learning-based SR methods were developed. Chen et al. [25] provided a trusted deep CNN-based SR method for HR medical image reconstruction, which can transmit the information of the output image to the low-level features by a feedback connection. Residual learning is a popular strategy in CNN-based SR algorithms, and it usually adopts the global residual learning (GRL) to model the residual image between the input interpolated LR image and the HR image. The GRL can learn details for SR in very deep convolutional networks [26]. Moreover, residual learning allows the idea of ‘the deeper, the better’ to still be true for SR because the residual network (ResNet) can solve the degradation problem in very deep networks to some extent [27], [28]. However, each fraction of a percent of improved accuracy usually requires nearly twice the number of network layers in ResNet [29]. Furthermore, Timofte et al. [30] invented generative adversarial network (GAN) and showed that fine grain texture and structure realism can be generated/recovered with supervision from a discriminator. Good-fellow et al. [31] introduced GAN in

This work was supported by National Natural Science Foundation of China (61871206, 61601450).

C. Yang, X. Liao, Y. Wang, M. Zhang, and Q. Liu are with the Department of Electronic Information Engineering, Nanchang University, Nanchang 330031, China. ({yangcailian, liaoxianghao}@email.ncu.edu.cn, {wangyuhao, zhangminghui, liuqiegen}@ncu.edu.cn).

SR task and GAN training has become popular in SR task [32]-[34]. For example, SRGAN [35], which was developed based on a GAN, had demonstrated perceptually better results compared to other deep residuals. Since there is no convergence guarantee for GAN, the stability of GAN has been an issue. Although there were plenty of decent SR results in the literature, bothersome artifacts or distortions were often observed in the SR results produced by these methods. Therefore, the challenge remains for achieving superior SR on MR images.

B. Review of PI

Parallel MRI (pMRI) is a robust way to accelerate data acquisition. The basis of pMRI is the simultaneous and independent data acquisition using receiver arrays with multiple radiofrequency coils. Scan time reductions are achieved by reducing the amount of gradient encoding steps normally required to obtain an artifact-free image. The reduced gradient encoding results in the under-sampling of k-space and hence produces aliasing artifacts. Dedicated pMRI algorithms such as simultaneous acquisition of spatial harmonics (SMASH) [36], sensitivity encoding (SENSE) [37], or generalized auto-calibrating partially parallel acquisitions (GRAPPA) [38] take advantage of spatial coil sensitivity variations to remove the aliasing artifacts.

The popular SENSE [37] approach is a pre-calibrated scheme that unfolds superimposed pixels by incorporating spatial coil sensitivity information. However, a challenge with calibration-based methods is the potential for motion artifacts, which results from mismatches between the calibration and main scans. In GRAPPA [38], missing k-space lines in a single-coil are approximated by a linear combination of measured k-space lines from all coils. To calculate the reconstruction coefficients, additional Nyquist sampled k-space lines (autocalibration signal, ACS) have to be measured. Recently, deep learning methods RAKI [39] and AC-LORAKS [40] that learn a neural network from the auto-calibration region have also been applied to improve the image quality at high acceleration factors. Despite these advances, the need to acquire fully sampled auto-calibration regions often restricts the achievable acceleration and the amount of higher k-space samples that can be acquired in a realistic scan time. To minimize these trade-offs, several researchers have exploited calibration-free approaches. Typical examples include simultaneous auto-calibrating and k-space estimation (SAKE) [41] as well as P-LORAKS [42]. Calibration-free techniques do not need specific calibration regions/pre-scans to estimate the interpolation kernels or sensitivities.

C. Contribution

In this article, we propose a method of using artificial intelligence to expand the channel, namely VCA. Specifically, we use dummy variable technology to expand the channel to achieve the effect of increasing the virtual coil. The main feature is the use of dummy variable technology to expand the channel in both the image and k-space domains. Although both are completed under a unified network framework, there are differences between them. The input and output of the image domain expansion are the data of the image domain, while the input and output of the k-space domain expansion are both the data of the k-space. The sum of squares (SOS) objective function of both VCA-I and VCA-K are executed in the image domain. Among them, the

channel expansion in the image domain has been published in the ICMIP conference [43] and an oral presentation has been made. In this paper, we have carried out more effective expansion on the original work.

The main contributions of this work are summarized as follows:

- To use the reversible network as the trained network, auxiliary variables technology is adopted to make the channel number of the network output to be equal to the network input. The variable enhancement technology provides higher-dimensional prior information for the network, which is helpful for the network to extract the deep feature information of the image.
- Channel expansion is performed in both the image and K-space domains, and the high-dimensional information formed by the channel expansion is used as the prior information of parallel imaging to improve the reconstruction effect.
- We propose to use the SOS objective function to solve the problem that k-space data is difficult to train and accelerate convergence. Simultaneously, we creatively propose that the input and output of VCA-K in training are both k-space domain data and the SOS objective function is performed in the image domain.

II. PRELIMINARY

A. Parallel MRI Reconstruction

Before discussing the details of the multiple coils, we first review some basics of PI technique. The formation of aliased images from multiple receivers in parallel MRI can be formulated as a linear operation to “fold” the full-FOV spin density images.

$$y = Ax \quad (1)$$

where y is the vector formed from the pixel intensities recorded by each receiver (folded image), and x is the vector formed from the full-FOV image. The encoding matrix A consists of the product of the aliasing operation due to sub-sampling of the k-space data and coil-specific sensitivity modulation over the image. The goal of the image reconstruction is to solve for x given our knowledge of A . In general, Eq. 1 is an over-determined linear system, i.e., the number of array coils, which is the row dimension of y , exceeds the number of the pixels that fold into the measured pixel, the row dimension of x . If the matrix is well conditioned, the inversion can be achieved with minimal amplification of noise. While the encoding matrix can still be inverted even if it is nearly singular, in this ill-conditioned case, small noise perturbations in the measured data (aliased image) can produce large variations in the full-FOV reconstruction. This effect causes noise amplifications in regions of the image where the encoding matrix is ill-conditioned.

To date, SENSE and GRAPPA remain the most common partially parallel imaging techniques. Both of these techniques increase imaging speed by reducing the number of phase encoding steps needed to encode an image. In SENSE, a set of N aliased images are acquired from an N -element receive array. The sensitivity patterns for each element in the array are adopted to form a set of linear equations which relate the aliased images from each coil to the unaliased full field-of-view image. Solving this set of equations performs an “unwrapping” of the data in the image domain to yield the desired image. In contrast to SENSE, GRAPPA methods

are not iterative and do not require prior knowledge of coil sensitivity profiles. Reconstruction is performed directly in k-space by estimating missing data points as weighted linear combinations of known acquired points. The GRAPPA weights implicitly contain information about the coil sensitivity profiles and are determined using one or more fully sampled training scans. Aliasing artifacts are caused by insufficient phase-encoding line sampling in k-space, while linear convolution kernels are susceptible to noisy methods at high acceleration factors. The coil sensitivity in the middle ACS line region is the most similar. Increasing the number of coils can reduce the image support, thereby alleviating the inverse problem of image reconstruction and promoting the improvement of imaging quality.

B. Hardware Multiple Coil

The idea of using an array of multiple and independent receive coils to reduce MR imaging time was first introduced in 1987 by two different groups [44], [45]. Indeed, Hutchinson and Raff went so far as to claim that a full $N \times M$ image could be acquired entirely without phase encoding by placing N closely spaced small receive coils around a sample [45]. The main problem with this completely parallel imaging method was that receiving an image from N receive coils required a receiver with at least N channels.

The idea of using multiple coils for imaging reconstruction has been the subject of some interest in the MRI community. The radio frequency coil of the system presented in [46] consists of four independent current sheet antennas. A head coil consisting of eight overlapping loop elements was used for imaging in [47]. A prototype of a degenerated birdcage resonator according to [48] for whole-body imaging was presented. Furthermore, Vernicke et al. [49] described the development of a multielement body coil with eight transmission electron microscope elements for application in a fully integrated multichannel MRI system. Massner et al. [50] proposed the concept of mechanically adjustable MR receiver coil arrays. An eight-channel wrist array for proton MRI at 3.0 T was constructed and evaluated. The array is adjusted to the individual anatomy by a mechanism that fitted a configuration of flexible coil elements closely around the wrist. Thalhammer et al. [51] introduced a 2D 16-channel receive coil array that is tailored for cardiac magnetic resonance imaging at 7.0 T. The coil array consists of two sections each using eight elements arranged in a 2×4 array. Graessl et al. [6] designed a modular transceiver coil array with 32 independent channels and received coil array for cardiac MRI at 7.0 T. The modular coil array comprises eight independent building blocks, each containing four transceiver loop elements. Keil et al. [7] designed a 64-channel brain array coil. The posterior former of the 64-channel array incorporated 39 hexagons and three pentagons; the anterior section contains 15 hexagons, three pentagons, two noncircular-shaped loops at the edge of the housing, and two somewhat oval-shaped eye loops.

These researches have shown that multiple coils have the potential for increasing the throughput of the MR imaging experiment via parallelization. Until recently, the number of independent receiver channels supported by MR systems was limited to typically 32 to 64. New spectrometer hardware is becoming available that permits 96 and more receiver channels to be used. This has triggered research into applying large coil arrays with up to 128 independent receive

channels. Fig. 1 shows eight-channel independent receiver MR systems. However, for large coil counts this is tedious to do in practice and requires cumbersome means of geometric fixation, which will often prove uncomfortable for the patient.

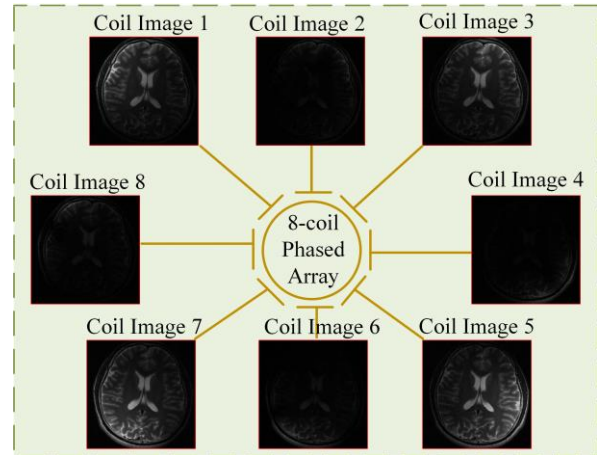


Fig. 1. An image obtained from an 8-coil phased array. Note Each coil is more sensitive to the signal from the tissue closest to it and can be used to form its image (small peripheral image). Independent coil images can be combined into a single image with uniform sensitivity.

C. Virtual Multiple Coil

These large physical coil arrays enable even faster data acquisition with high SNR. However, their construction and data storage of these large datasets are becoming increasingly problematic. To further improve the effect of parallel imaging, some researchers have proposed the concept of virtual coils [52], [53]. Generating additional data in the form of virtual coils is an efficient way to improve pMRI reconstructions. For example, Liao et al. [54] proposed a virtual coil (VC) reconstruction framework to improve highly accelerated single-shot echo planar imaging (EPI) and generalized slice dithered enhanced resolution acquisition in high-resolution diffusion imaging. However, VC requires the phase to be consistent between the reference data and imaging data. Blaimer et al. [52] presented a new approach for utilizing conjugate k-space symmetry for improved parallel MRI performance. By generating virtual coils containing conjugate symmetric k-space signals from actual coils, additional image-phase and coil-phase information can be incorporated into the reconstruction process for parallel acquisition techniques. Besides, VCC-GRAPPA [55] combines the virtual conjugate coil concept with k-space algorithms (GRAPPA and ESPIRiT) for image reconstruction. Extra spatial encoding capability provided by the phase map of VCC would result in improved GRAPPA inverting conditions. In addition, Wang et al. proposed NL-VCC-GRAPPA [57] to jointly utilize the nonlinear mapped virtual coil and phase conjugated virtual coil to further reduce noise amplification in parallel imaging. The idea of virtual coil has been generalized by Bilgic et al. [56] from VCC to further utilize information redundancy from the multi-contrast, multi-echo, or phase cycled BSSFP datasets to improve the pMRI reconstruction condition. Very recently, Liu et al. [58] combined single-shot variant EPI (ssDW-EPI) with virtual coil acquisition and develop a self-reference reconstruction method to eliminate the residual aliasing artifact on multi-oblique ssDW-EPI sequence with parallel imaging and multiple signals averaging.

Since the position of the coil is different concerning the

imaging site, the sensitivity of each coil to the imaging site is also different. The signal intensity obtained by the part with high sensitivity is high, and the finally obtained image is brighter. Otherwise, the signal strength is small, and the final image obtained is relatively dark. Each coil can be used to form its image, and then the independent coil images can be combined into an image with uniform sensitivity through the square sum operation. The basic concept of virtual coils is to generate redundant coils through deep learning, and simulate physical coils through the generated virtual coils. Fig. 2 demonstrates virtual coil technology. Specifically, the 4-channel independent receiving system collects signals, and the data of 8-channel or even more channels can be simulated through deep learning.

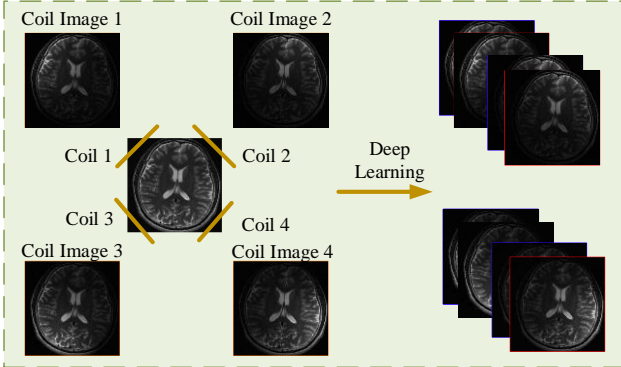


Fig. 2. The virtual coils technology. The image in the red-square box is the generated virtual coil.

III. PROPOSED VCA MODEL

In the previous section, we discussed the basics of parallel imaging, hardware multi-coil, and virtual multi-coil. In this section, we mainly introduce the proposed channel expansion method and its difference in image domain and k-space domain. The network structure and loss function of the proposed method are also presented in this part. Particularly, this article uses variable enhancement technology to expand the channel in the image domain and k-space domain to tackle the problem of low image resolution and slow imaging speed.

A. Proposed VCA

As we all know, MR image is different from natural image, which is a complex-valued image. Thus, 12-channels 256×256 complex-valued images x are used as the training and testing data of our model. Since the input images are complex-valued, each channel with complex value can be represented by 2-channels with real value, which contains real and imaginary components, respectively. Hence, we acquire 24-channels 256×256 input images X of the same dimension by decomposing complex-valued images into real and imaginary components. In other words, $X = \{[x_{real1}, x_{imag1}], \dots, [x_{realn}, x_{imagn}]\}$ is used as the input of the network.

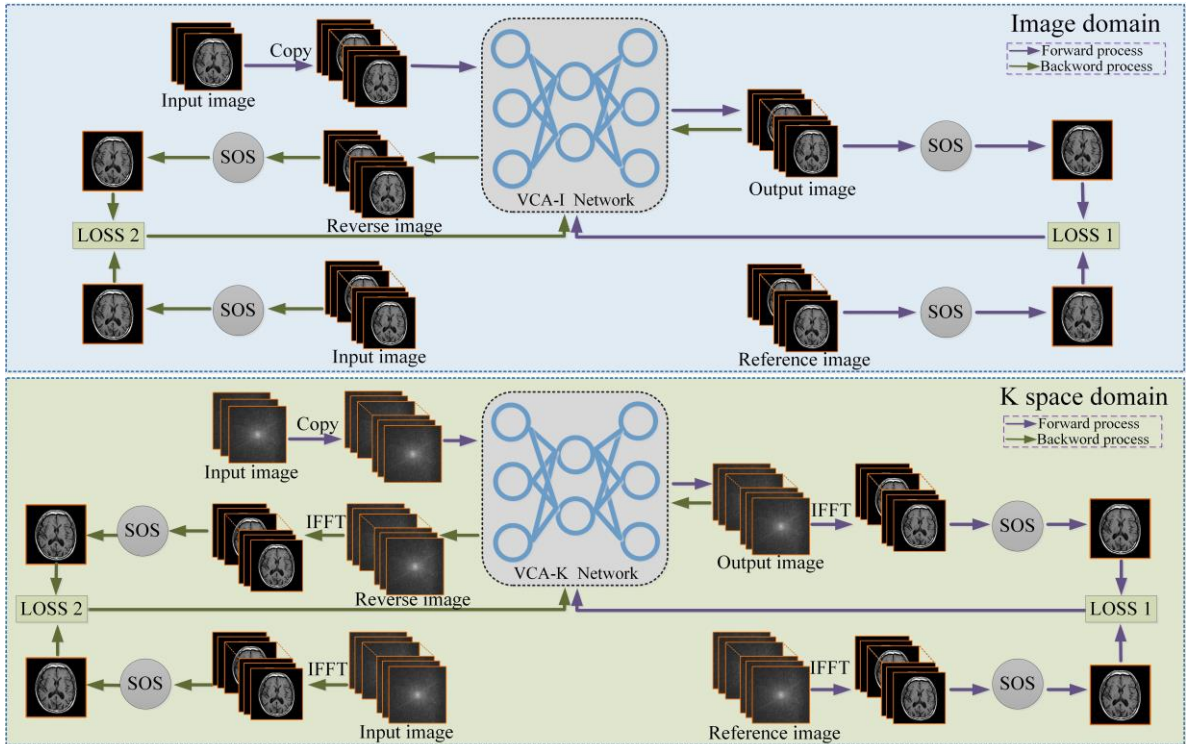


Fig. 3. The training pipeline of VCA. The top part is the channel expansion method in the image domain, and the bottom part is the channel expansion method in the k-space domain. Among them, variable enhancement technology is used in the process of image pre-processing. The loss function is composed of a forward loss function and a reverse loss function. For the convenience of readers, the detailed architecture of VCA is described in Section III. B. On the other hand, the description of the loss functions in the training objectives is provided in Section III. C.

Reversible network is applied as the training network of VCA for reconstruction. Specifically, the model is designed with the composition of a stack of affine coupling layers and utilizes the invertible 1×1 convolution as the learnable permutation function between the coupling layers. Note that the channel number of network input and output must be equal,

due to the invertible convolution and connection operations. In this study, inspired by the work in [59], we use dummy variable technology to increase the channel dimensions to make the number of input and output channels of the reversible network consistent. Specifically, we copy 2-channel complex image into a 12-channel complex image, which is

stacked into 24-channel as the input of the network, and the output of the network is also 24-channel. Finally reconstructed images can be obtained after SOS.

During the training, the difference between reconstructed images and ground truth images is not only applied to adjust reconstruction layer to restore better images from manifold, but also to guide extraction of accurate image features. The top part of Fig. 3 is the channel expansion method in the image domain, and the bottom part is the channel expansion method in the k-space domain. Among them, variable enhancement technology is utilized in the process of image preprocessing. A combination of the forward loss and backward loss is employed to optimize VCA.

Although VCA-I and VCA-K are completed under a unified network framework, there are differences between the two. The input and output of the image domain expansion are the data of the image domain, while the expansion input and output of the k-space domain are both the data of the k-space. The SOS objective function of both VCA-I and VCA-K are executed in the image domain. As we all know, the k-space samples are in the spatial frequency domain. Because the amplitude difference in the magnetic resonance k-space is too large, and it is impossible to train a better model by directly calculating the objective function in the frequency domain. Therefore, VCA-K calculates the objective function in the image domain, so that the features can be extracted well in the network training process, and at the same time, the SOS is used to further improve the network performance.

B. Network Architecture

Our goal is to find a bijective function which can map the data point from input data space X to output data space Y . To achieve this, classical neural networks need two separate networks to approximate $X \rightarrow Y$ and $Y \rightarrow X$ mappings respectively, which leads to inaccurate bijective mapping and may accumulate the error of one mapping into the other. We take an alternative method and use the affine coupling layers in [60], [61] to enable the invertibility of one single network.

We design our VCA with the composition of a stack of invertible and tractable bijective functions $\{f_i\}_{i=0}^k$, i.e., $f = f_0 \circ f_1 \circ f_2 \circ \dots \circ f_k$. For an image pair (x, y) , with only one invertible network f , inputting the image x into the network yields the output image y and vice versa. Thus, the information is fully preserved during both the forward and reverse transformations. We can derive the transformation to target data sample y through:

$$y = f_0 \circ f_1 \circ f_2 \circ \dots \circ f_k(x) \quad (2)$$

$$x = f_k^{-1} \circ f_{k-1}^{-1} \circ \dots \circ f_0^{-1}(y) \quad (3)$$

The bijective model f_i is implemented through affine coupling layers. The affine coupling layer provides a powerful reversible transformation where the forward function, the reverse function and the log-determinant are computationally efficient. In each affine coupling layer, given a D dimensional input m and $d < D$, the output n is calculated as:

$$n_{1:d} = m_{1:d} \quad (4)$$

$$n_{d+1:D} = m_{d+1:D} \odot \exp(s(m_{1:d})) + t(m_{1:d}) \quad (5)$$

where s and t represent scale and translation functions from $R^d \rightarrow R^{D-d}$, and \odot is the Hadamard product. Note that the scale and translation functions are not necessarily

invertible, and thus they are realized by a succession of several convolution layers with leaky ReLU activations.

As stated in [61], the coupling layer leaves some input channels unchanged, which greatly restricts the representation learning power of this architecture. To alleviate this problem, we firstly enhance [62] the coupling layer by:

$$n_{1:d} = m_{1:d} + r(m_{d+1:D}) \quad (6)$$

where r can be an arbitrary function from $R^{D-d} \rightarrow R^d$. The inverse step is easily obtained by:

$$m_{d+1:D} = (n_{d+1:D} - t(n_{1:d})) \odot \exp(-s(n_{1:d})) \quad (7)$$

$$m_{1:d} = n_{1:d} - r(m_{d+1:D}) \quad (8)$$

Each step of flow should be preceded by some kind of permutation of the variables that ensures that after sufficient steps of flow, each dimension can affect every other dimension. Next, we utilize the invertible 1×1 convolution proposed in [60] as the learnable permutation function to reverse the order of channels for the next affine coupling layer. The weight matrix is initialized as a random rotation matrix. Note that a 1×1 convolution with the equal number of input and output channels is a generalization of a permutation operation.

The elaborate architecture of VCA is shown in Fig. 4. It contains several invertible blocks, where each invertible block consists of invertible 1×1 convolution and affine coupling layers. The split function splits the input tensor into two halves along the channel dimension, while the concat operation performs the corresponding reverse operation: concatenation into a single tensor. In [63], another type of split was introduced: along the spatial dimensions using a checkerboard pattern. In this work we only perform splits along the channel dimension, simplifying the overall architecture. s , t and r are transformation equal to dense block, which consists of five 2D convolution layers with filter size 3×3 . Each layer learns a new set of feature maps from the previous layer. The size of the receptive field for the first four convolutional layers is 3×3 , and stride is 2, followed by a rectified linear unit (ReLU). The last layer is a 3×3 convolution without ReLU. The purpose of the Leaky ReLU layers is to avoid overfitting to the training set [64] and further increase nonlinearity. Invertible model is composed of both forward and inverse processes. During the training time, the input image is transformed to output images of reconstruction by a stack of bijective functions $\{f_i\}_{i=0}^k$.

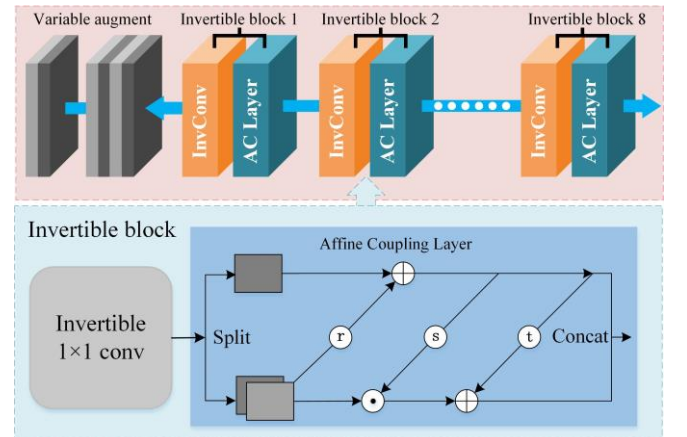


Fig. 4. The pipeline of VCA. Invertible model is composed of both forward and inverse processes. We illustrate the details of the invertible block on the bottom. r , s , and t are transformations defined in the bijective functions $\{f_i\}_{i=0}^k$.

C. Training Objectives

For obtaining visually pleasing reconstructed images, we conduct bi-directional training with smooth L_1 loss. The gradient of smooth L_1 loss function is constant when x is large, which solves the problem of large gradient in L_2 loss that destroys training parameters. When x is small, the gradient will dynamically decrease, which tackles the problem of difficulty in convergence in L_1 loss. It is worth noting that although VCA-I and VCA-K are performed in the image domain and k-space domain individually, the SOS and loss functions of both VCA-I and VCA-K are performed in the image domain. Therefore, the network output image and label image of VCA-K need inverse Fourier transform before calculate the loss function.

The bi-directional loss function consists of forward loss L_f and backward loss L_r . VCA model optimizes the total loss L by conducting joint training on the two following objectives:

$$L = \alpha L_f + \beta L_r \quad (9)$$

where α and β are coefficients for balancing different loss terms. Given d , it represents the error between predicted value and ground truth. The smooth L_1 is defined as

$$\text{smooth}_{L_1}(d) = \begin{cases} 0.5d^2 & \text{if } |d| < 1 \\ |d| - 0.5 & \text{otherwise} \end{cases} \quad (10)$$

The output of variable augmented invertible network is given as $\hat{x}_k = \{\hat{x}_1, \hat{x}_2, \dots, \hat{x}_i\}$. The forward process can be expressed as:

$$L_f = \|SOS(x) - SOS(\hat{x}_k)\|_1^{\text{smooth}} \quad (11)$$

where SOS is defined as $y = (\sum_{k=1}^N |X_k|^2)^{1/2}$, X_k is the complex-valued image from channel K , and x denotes label images. The backward process can be expressed as:

$$L_r = \|SOS(x) - SOS(\hat{x})\|_1^{\text{smooth}} \quad (12)$$

where \hat{x} denotes the reversed result images.

IV. EXPERIMENTS

In this section, we introduce the implementation details of the proposed VCA, as well as the datasets we use for evaluation. Subsequently, we not only perform an ablation experiment in the image domain and compare it with the SR algorithm, but also conduct ablation experiments in the k-space domain and perform parallel imaging reconstruction on the dataset after the channel expansion.

A. Experiment Setup

Datasets. We use two datasets to evaluate VCA, which are provided by Shenzhen Institutes of Advanced Technology, the Chinese Academy of Science. First, the Brain data are scanned from a 3T Siemens's MAGNETOM Trio scanner using the T2-weighted turbo spin echo sequence. 480 MR images with 12-channels are chosen as the training data and 20 images are selected as validation data. The relevant imaging parameters include the size of image acquisition matrix is 256×256 , echo time (TE) is 149 ms, and repetition time (TR) is 2500 ms. The FOV is $220 \times 220 \text{ mm}^2$ and the slice thickness is 0.86 mm. Second, 101 fully-sampled Cardiac MR images are acquired with T1-weighted FLASH

sequences via using 3T MRI scanner (Siemens's MAGNETOM Trio), which receiver coils number is 20. We select 21 MR images as the verification dataset. Typically, the TR/TE is 5/3 ms; acquisition matrix size is 216×216 ; FOV is $330 \times 330 \text{ mm}^2$, and slice thickness is 6 mm. Our architecture uses 2D axial-plane slices of the volumes as the network input. For each volume, we linearly scale the original intensity values to $[-1, 1]$. To increase the number of training samples, we rotate the original image by different angles.

Model Training. All networks are trained using the Adam solver. We conduct 300 epochs to train the proposed model. The initial learning rate is set to 0.0001 for the first 50 epochs. Every 50 epochs the learning rate is halved to achieve optimal results. During training, the trade-off parameter α and β are set to 12 and 1. Data augmentation is performed on the training images, which are randomly rotated by 90° , 180° , 270° and flipped horizontally to obtain more training data. The training and testing experiments are performed with a customized version of Pytorch on an Intel i7-6900K CPU and a GeForce Titan XP GPU. For the convenience of reproducible research, source code of VCA can be downloaded from the website: <https://github.com/yqx7150/VCA>.

Quality Metrics. To evaluate the quality of the reconstructed images, two metrics, the popular peak signal to noise ratio (PSNR) and the powerful perceptual quality metrics structural similarity (SSIM) are selected for quantitative assessment.

Specifically, the PSNR describes the relationship of the maximum possible power of a signal with the power of noise corruption. Higher PSNR means better image quality. Denoting x and \hat{x} to be the reconstructed image and ground truth, PSNR is expressed as:

$$\text{PSNR}(x, \hat{x}) = 20 \log_{10} [\text{Max}(\hat{x}) / \|x - \hat{x}\|_2]. \quad (13)$$

The SSIM was used to measure the similarity between the original MRI image and reconstructed images, evaluated on three aspects: luminance, contrast, and structural correlation. SSIM values are normalized between 0 and 1. SSIM is defined as:

$$\text{SSIM}(x, \hat{x}) = \frac{(2\mu_x \mu_{\hat{x}} + c_1)(2\sigma_{x\hat{x}} + c_2)}{(\mu_x^2 + \mu_{\hat{x}}^2 + c_1)(\sigma_x^2 + \sigma_{\hat{x}}^2 + c_2)} \quad (14)$$

where μ_x and σ_x^2 are the average and variances of x . $\sigma_{x\hat{x}}$ is the covariance of x and \hat{x} . c_1 and c_2 are used to maintain a stable constant.

B. Ablation Study in Image Domain

The SCC [65] and GCC [66] algorithm can be used for image compression in the image domain as well as in the k-space domain. In the experiments, we use the SCC algorithm to compress the 12-channel Brain dataset and the 20-channel Cardiac dataset into two channels as input for training. The brain dataset was compressed into 4-channel and 6-channel using the GCC algorithm, while the heart dataset was compressed into 6-channel and 10-channel as label images. A higher number of ACS lines with an auto-calibrated signal produces better compressed data, but requires a longer compression time. The number of ACS lines is selected as 24 for image compression in our experiment.

To verify the effect of virtual coils, we copy the two-channel image into different channels through variable enhancement technology for reconstruction. To show a clearer

visual effect, we demonstrate the residual results of the reference image and the reconstructed image in Fig. 5 and Fig. 6. Visually, the proposed VCA-I algorithm has achieved good reconstruction results in different channel expansions. In particular, the reconstruction results of the 12-channel Brain image and the 20-channel Cardiac image are sharpest and closest to ground truth images. Quantitatively, we calculate SSIM and PSNR metrics between output and ground truth images and report the number in Table.1. VCA-I obtains high results in all two indexes. The average PSNR of VCA-I can reach 39 dB and 25.12 dB on two datasets, respectively. As the number of channels increases, the effect of reconstruction after SOS is better. In other words, VCA-I

enhances the correlation of data through virtual coils technology, which is conducive to the formation of characterization information, thereby improving the reconstruction results.

Table. 1 Quantitative reconstruction (PSNR/SSIM) results for VCA-I on Brain and Cardiac datasets.

Brain	2ch → 4ch	2ch → 6ch	2ch → 12ch
	37.27/0.9880	38.84/0.9869	41.00/0.9887
Cardiac	2ch → 6ch	2ch → 10ch	2ch → 20ch
	24.79/0.8814	25.12/0.8817	25.45/0.8771

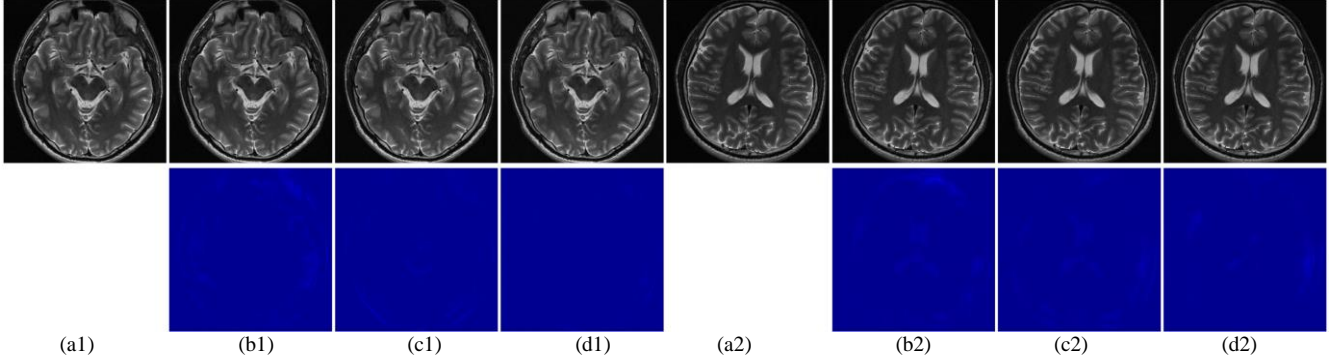


Fig. 5 Reconstruction results of Brain dataset for VCA-I. Top: (a) Reference image of Brain dataset; Reconstruction result of (b) 2ch → 4ch; (c) 2ch → 6ch (d) 2ch → 12ch; Bottom: The residuals between the reference images and reconstruction images.

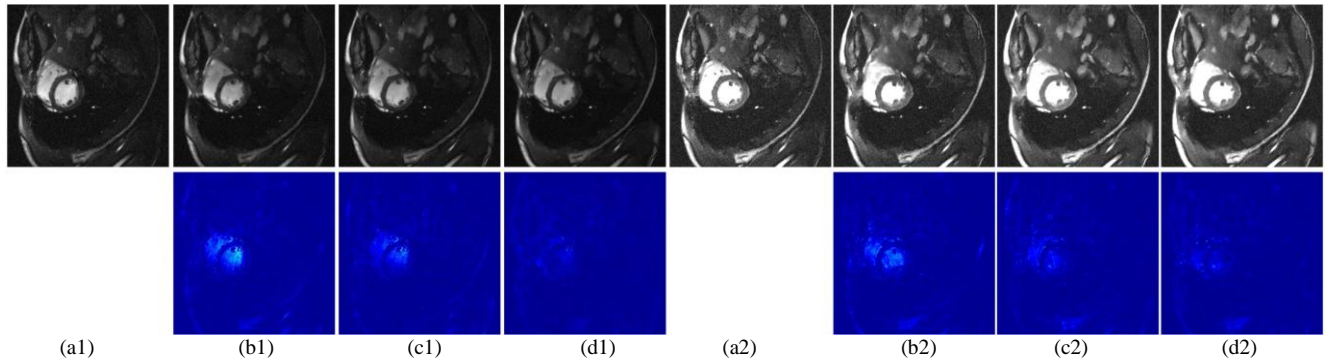


Fig. 6 Reconstruction results of Cardiac dataset for VCA-I. Top: (a) Reference image of Cardiac dataset; Reconstruction result of (b) 2ch → 6ch; (c) 2ch → 10ch (d) 2ch → 20ch; Bottom: The residuals between the reference images and reconstruction images.

C. SR Comparison in Image Domain

In this part, we compare our algorithm with four state-of-the-art SR methods. These well-known benchmark SR methods include BICUBIC [18], SRCNN [23], FAWDN [25], and SRGAN [35]. Among them, BICUBIC is the traditional interpolation method. SRCNN is the earliest proposed SR algorithm based on CNN, which directly learns the end-to-end mapping from LR images to HR images. FAWDN is a deep convolutional neural network-based SR method for HR medical image reconstruction. SRGAN is a typical GAN-based SR algorithm. In our experiments, the networks of all the algorithms are retrained for database. Two images with sufficient texture details were selected from the testing set to show the performance of each SR method. The comparisons between the high-resolution images obtained by each method and the real high-resolution images (Ground

Truth, GT) are shown in Fig. 7.

Encouragingly, our method outperforms these methods as evidenced by the resultant SR images with higher PSNR and SSIM values. For instance, our algorithm can reach 41 dB, which is 11.54 dB, 9.1 dB, 6.99 dB, and 8.64 dB higher than BICUBIC, SRCNN, FAWDN, and SRGAN algorithms, respectively. Compared with SRGAN, the most distinct characteristic of VCA-I is that artifacts and noise are greatly reduced. Also, VCA-I shows richer textural details than FAWDN and SRCNN. Since interpolations do not introduce any new details into the enlarged images, Bicubic easily produces ringing and excessive smoothing. For example, from the residual image in Fig. 5, it is observed that the texture details of VCA-I are clearer and closer to the ground truth, and these textures are blurred in the images generated by other methods.

Table. 2 Comparison results with four state-of-the-art methods on Brain dataset in terms of PSNR and SSIM.

Dataset	BICUBIC	SRCNN	FAWDN	SRGAN	VCA-I
Brain	29.46/0.8967	31.90/0.9316	34.01/0.9356	32.36/0.9354	41.00/0.9887

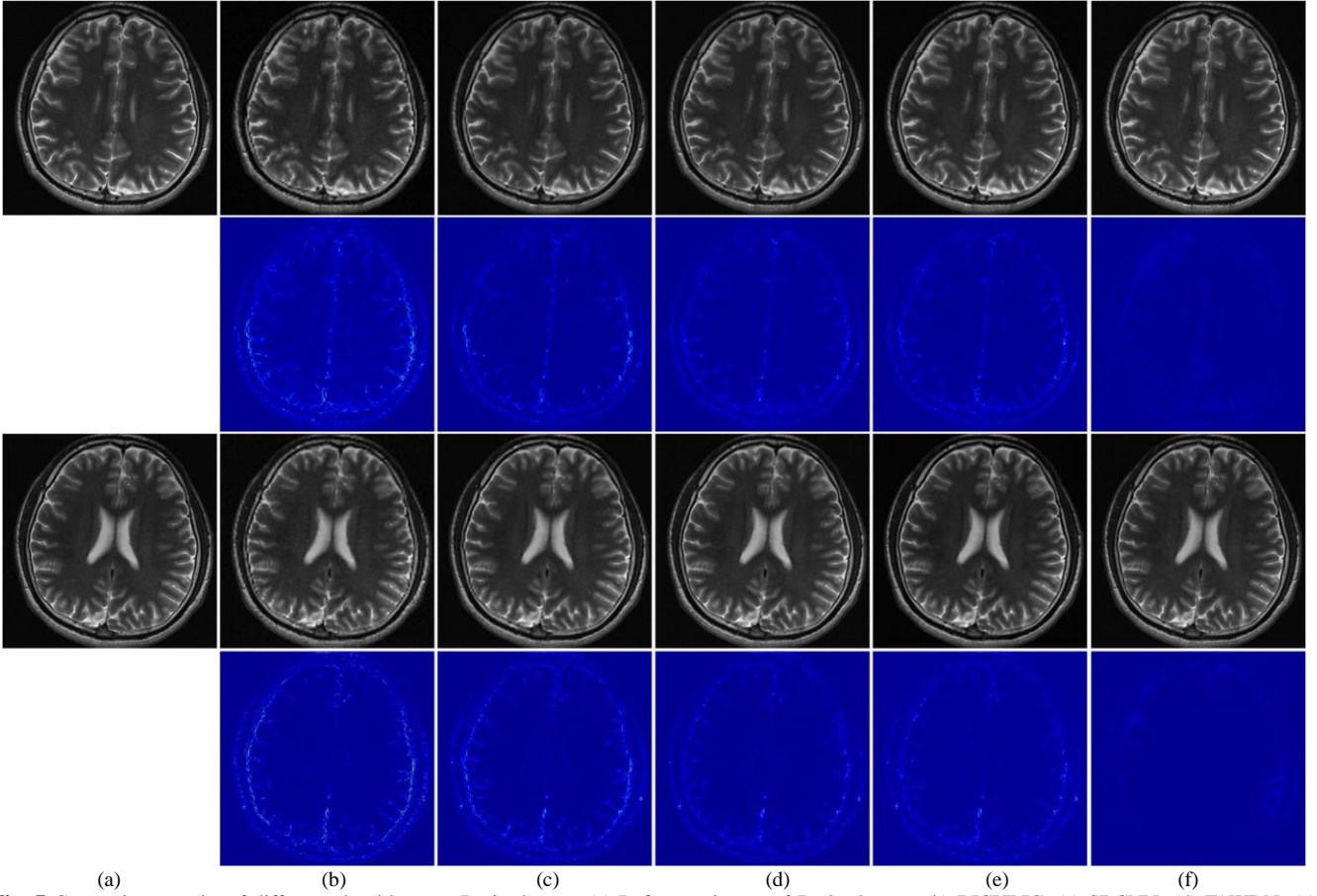


Fig. 7 Comparison results of different algorithms on Brain dataset. (a) Reference image of Brain dataset; (b) BICUBIC; (c) SRCNN; (d) FAWDN; (e) SRGAN; (f) VCA-I; Bottom: The residuals between the reference images and reconstruction images.

D. Ablation Study in K -space Domain

To evaluate the effectiveness of virtual coils technology, we carry out ablation studies. We use SCC [65] to generate two-channel images from the original images. The dataset in the k -space domain is obtained through the Fourier transform of the image domain dataset. Taking the brain dataset as an example, two-channel k -space complex images are used as the input of the network. At the same time, the data of 4 channels, 6 channels and 12 channels are used as labels to verify the effect of multi-channel. It is noteworthy that the loss function of VCA-K is performed in the image domain.

Table 3 shows the reconstructed PSNR and SSIM of VCA-K can reach 42.47 dB and 0.9874 on the Brain dataset. The 12-channel Brain dataset is 2.5 dB and 4.5 dB higher than the 6-channel Brain dataset and the 4-channel Brain

dataset, separately. In the Cardiac dataset, the PSNR of the reconstruction results increases after channel augmentation compared to the two-channel dataset. Qualitatively, the same conclusion can be obtained from Fig. 8 and Fig. 9. It is consistent with the results obtained in the image domain. Thus, it proves that our algorithm not only has a better reconstruction effect in the image domain as the number of channels increases, but also in the k -space domain.

Table. 3 Quantitative reconstruction (PSNR/SSIM) results for VCA-K on Brain and Cardiac datasets.

Brain	2ch \rightarrow 4ch	2ch \rightarrow 6ch	2ch \rightarrow 12ch
	37.97/0.9761	39.93/0.9852	42.47/0.9874
Cardiac	2ch \rightarrow 6ch	2ch \rightarrow 10ch	2ch \rightarrow 20ch
	23.16/0.8259	23.15/0.8119	23.07/0.8157

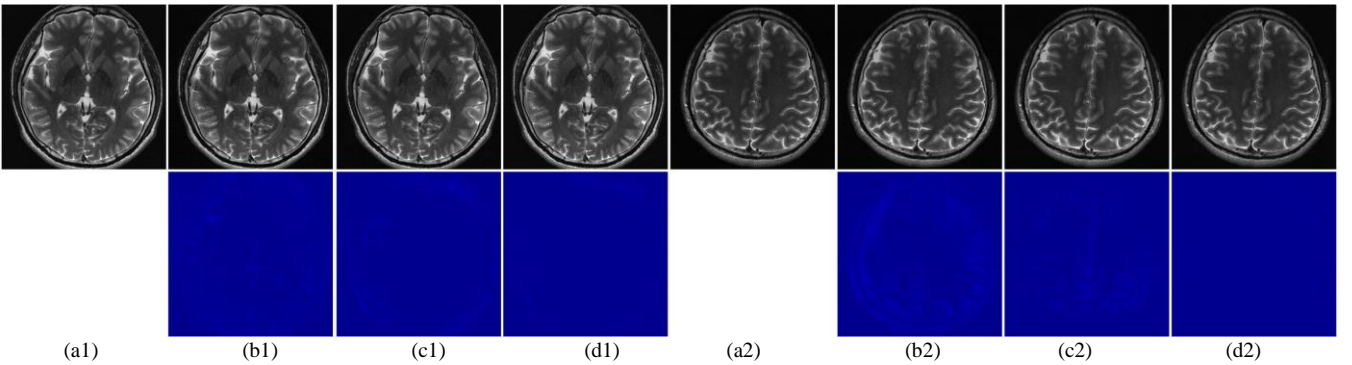


Fig. 8 Reconstruction results of Brain dataset for VCA-K. Top: (a) Reference image of Brain dataset; Reconstruction result of (b) 2ch \rightarrow 4ch; (c) 2ch \rightarrow 6ch (d) 2ch \rightarrow 12ch; Bottom: The residuals between the reference images and reconstruction images.

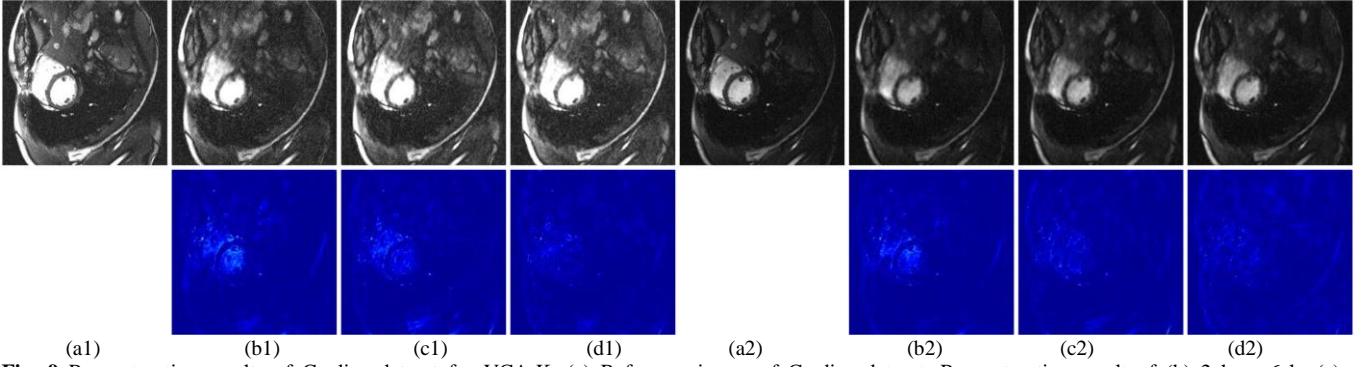


Fig. 9 Reconstruction results of Cardiac dataset for VCA-K. (a) Reference image of Cardiac dataset; Reconstruction result of (b) 2ch \rightarrow 6ch; (c) 2ch \rightarrow 10ch (d) 2ch \rightarrow 20ch; Bottom: The residuals between the reference images and reconstruction images.

E. PI Comparison in K -space Domain

To further evaluate the proposed method, we compare the reconstruction effects of parallel imaging algorithm before and after the channel expansion under different acceleration factors. We use three representative parallel imaging methods, which span various reconstruction classification models, including ESPIRiT [67], L_1 ESPIRiT [68] and AC_LORAKS [40]. The experiment is conducted under-sampling at equal intervals with acceleration factor of 2, 3, 4, and 5. The number of reference lines for auto-calibration and the calculation of the coil sensitivity profiles is 30. The

data employed to construct calibration matrix is $256 \times 30 \times 12$, and the kernel size (window size) is 6×6 . Here, a lower threshold of 0.02 is used for calculation of the sensitivity maps to avoid truncation artifacts. We take ESPIRiT as an example to describe the reconstruction steps using parallel imaging algorithms after channel expansion. At the first step, virtual coils are formed for both ACS and under-sampled data according to variable augmentation technology. In the second step, a standard ESPIRiT reconstruction is performed and the resulting images are combined using SOS.

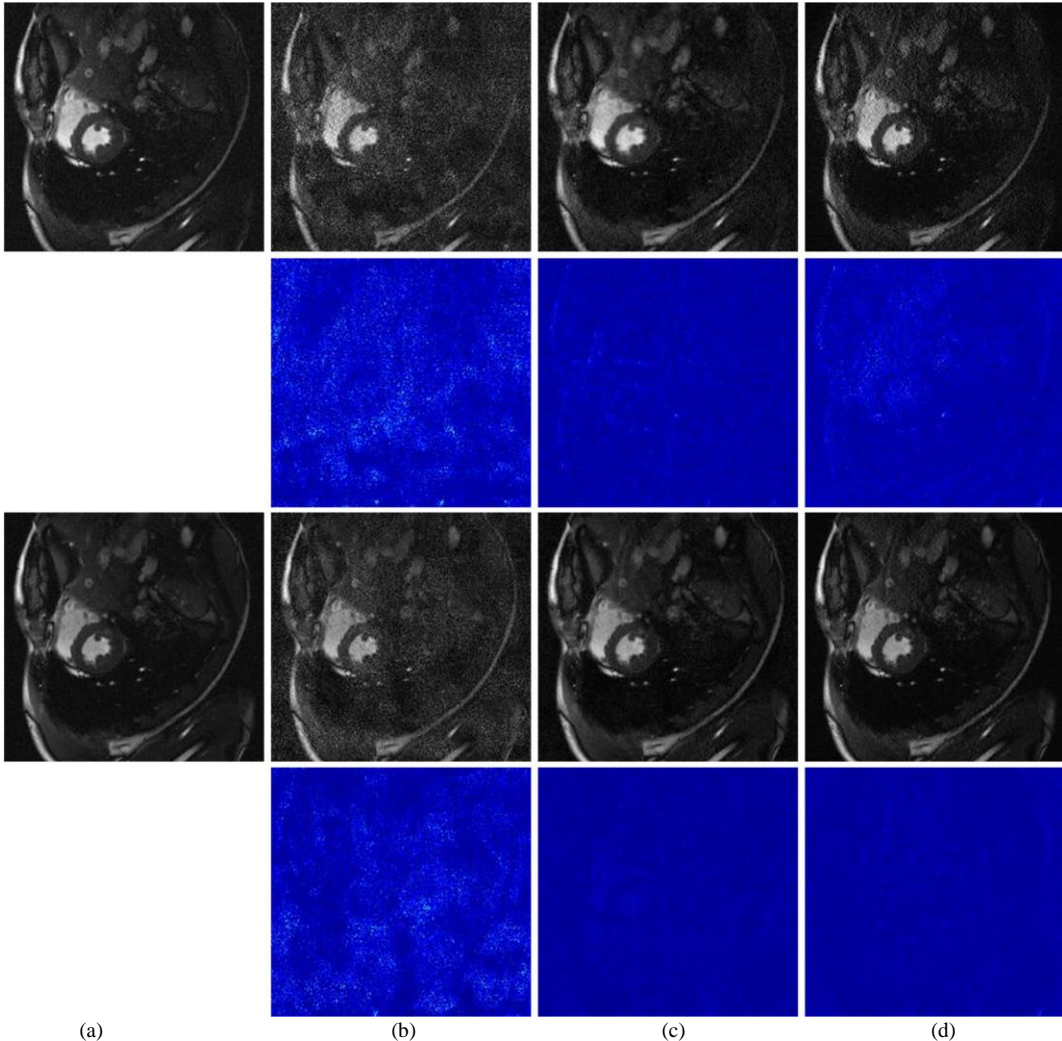


Fig. 10 Comparison results of the 20-coil after channel expansion and the original 6-coil at an acceleration factor of 4. (a) Reference image of Cardiac dataset; (b) ESPIRiT; (c) L_1 ESPIRiT; (d) AC_LORAKS; The first row is the original 6-coil, and the third row is the reconstruction effect of the expanded 20-coil. The second and fourth rows are residuals between the reference images and reconstruction images.

We use the high-dimensional information formed by channel expansion as the prior information of parallel imaging to improve the reconstruction effect of parallel imaging. The result before channel expansion is calculated using 6 channels of under-sampled data as input and 6 channels of fully sampled data as labels. The result after channel expansion is calculated by using the expanded 20-channel under-sampled data as the input and using the 20-channel full-sampled data as the label. Image reconstruction performance comparisons under different sampling rates for Cardiac dataset are summarized in Table 4. Specifically, the PSNR and SSIM of the three algorithms are improved at different sampling rates. Due to the k-space is variable density randomly under-sampled, it tends to produce structure-like artifacts.

Visually, the performances of reconstruction for different methods are various. It is worth noting that the three reconstruction methods are significantly improved after channel expansion. It can also be seen from the residual that the reconstruction effect after channel replication is better than the previous reconstruction effect. Since, extra information provided by the virtual coils is available for synthesizing the target signal, thereby improving the reconstruction conditions and image quality. It further proves that our algorithm can not only improve the image reconstruction quality in the case of full sampling, but also contribute to the further reconstruction of the parallel imaging algorithm in the case of under-sampling.

Table. 4 Comparison results of 20-coil after channel expansion and the original 6-coil with three state-of-the-art methods in terms of PSNR and SSIM.

Dataset		ESPIRIT	L_1 ESPIRIT	AC_LORAKS
R=2	6 coils	21.9156/0.4320	30.6813/0.7706	32.1488/0.8396
	6 coils→20 coils	25.0745/0.5510	33.5023/0.8527	35.5668/0.9146
R=3	6 coils	21.2200/0.3845	29.0514/0.7008	28.6818/0.7246
	6 coils→20 coils	24.0622/0.5024	32.6230/0.8294	32.8696/0.8610
R=4	6 coils	21.6511/0.3732	28.1578/0.6790	27.0052/0.6483
	6coils→20 coils	24.0158/0.4978	31.7909/0.8059	31.2458/0.8116
R=5	6 coils	22.2270/0.3877	27.7027/0.6648	24.9026/0.5742
	6 coils→20 coils	24.1863/0.4886	30.9807/0.7864	29.7043/0.7561

V. CONCLUSIONS

In this paper, we propose a method of using artificial intelligence to expand the channel. We use a reversible network as a training network, and use auxiliary variable technology to make the number of channels output by the network equal to the input of the network. Increasing the channel information through the virtual variable enhancement technology to achieve the effect of increasing the virtual coil. We creatively proposed a method of training in the k-space domain and loss function in the image domain. VCA can not only expand the channel in the image domain, but also expand the channel in the k-space domain. The main advantage of VCA-K is the easy implementation for improved parallel MRI performance without requiring modifications of the reconstruction algorithms. Comparative experiments demonstrate that VCA could obtain more clear and trusted medical images than state-of-the-art methods.

REFERENCES

- [1] P. B. Roemer, W. A. Edelstein, C. E. Hayes, S. P. Souza, and O. M. Mueller, "The NMR phased array," *Magn. Reson. Med.*, vol. 16, pp. 192-225, 1990.
- [2] E. B. Boskamp, "A new revolution in surface coil technology: the array surface coil," *In: Proceedings of the 6th Annual Meeting of ISMRM*, p.405, 1987.
- [3] C. E. Hayes, N. Hattes, and P. B. Roemer, "Volume imaging with MR phased arrays," *Magn. Reson. Med.*, vol. 18, pp. 309-319, 1991.
- [4] S. M. Wright, R. L. Magin, and J. R. Kelton, "Arrays of mutually coupled receiver coils: theory and application," *Magn. Reson. Med.*, vol. 17, pp. 252-268, 1991.
- [5] P. B. Roemer, W. A. Edelstein, C. E. Hayes, S. P. Souza, and O. M. Mueller, "The NMR phased array," *Magn. Reson. Med.*, vol. 16, pp. 192-225, 1990.
- [6] A. Graessl, W. Renz, F. Hezel, M. A. Dieringer, and L. Winter et al., "Modular 32-channel transceiver coil array for cardiac MRI at 7.0T," *Magn. Reson. Med.*, vol. 72, pp. 276-290, 2013.
- [7] B. Keil, J. N. Blau, S. Biber, P. Hoecht, and V. Tountcheva et al., "A 64-channel 3T array coil for accelerated brain MRI," *Magn. Reson. Med.*, vol. 70, pp. 248-258, 2012.
- [8] G. C. Wiggins, A. Potthast, and C. Triantafyllou, et al., "A 96-channel MRI system with 23- and 90-channel phase array head coils at 1.5 Tesla," *In: Proceedings of the 13th Annual Meeting of ISMRM*, 2005.
- [9] G. C. Wiggins, V. Alagappan, and A. Potthast, et al., "Design optimization and SNR performance of 3T 96 channel phased array head coils," *In: Proceedings of the 15th Annual Meeting of ISMRM*, 2007.
- [10] C. Hardy, R. Giaquinto, and J. Piel, et al., "128-channel body MRI with a flexible high-density receiver-coil array," *In: Proceedings of the 15th Annual Meeting of ISMRM*, 2007.
- [11] M. Schmitt, A. Potthast, D. E. Sosnovik, G. C. Wiggins, and C. Triantafyllou et al., "A 128 channel receive-only cardiac coil for 3T," *In: Proceedings of the 15th Annual Meeting of ISMRM*, 2007.
- [12] S. Vasanawala, T. Grafendorfer, P. Calderon, G. Scott, and M. Alley, et al., "Millimeter isotropic resolution volumetric pediatric abdominal MRI with a dedicated 32 channel phased array coil," *In Proceedings of the 19th Annual Meeting of ISMRM*, p. 161, 2011.
- [13] Y. Zhu, C. Hardy, D. Sodickson, R. Giaquinto and C. Dumoulin, et al., "Highly parallel volumetric imaging with a 32-element RF coil array," *Magn. Reson. Med.*, vol. 52, pp. 869-877, 2004.
- [14] M. McDougall, S. Wright, "64-channel array coil for single echo acquisition magnetic resonance imaging," *Magn. Reson. Med.*, vol. 54, pp. 386-392, 2005.
- [15] M. Schmitt, A. Potthast, D. Sosnovik, J. Polimeni and G. Wiggins et al., "A 128-channel receive-only cardiac coil for highly accelerated cardiac MRI at 3 Tesla," *Magn. Reson. Med.*, vol. 59, pp. 1431-1439, 2008.
- [16] S. C. Park, M. K. Park, and M. G. Kang, "Super-resolution image reconstruction: a technical overview," *IEEE Signal Process. Mag.*, vol. 20, no. 3, pp. 21-36, 2003.
- [17] X. Li, et al., "New edge-directed interpolation," *IEEE trans. image process.*, vol. 10, no. 10, pp.1521-1527, 2001.
- [18] R. Keys, "Cubic convolution interpolation for digital image processing," *IEEE Trans. Acoust. Speech Signal Process.*, vol. 29, no. 6, pp.1153-1160, 1981.
- [19] R. Hardie, "A fast image super-resolution algorithm using an adaptive Wiener filter," *IEEE trans. image process.*, pp.2953-2964, 2007.
- [20] J. V. Manjón, et al., "Non-local MRI up-sampling," *Med. Image Anal.*, pp.784-792, 2010.
- [21] J. Yang, et al., "Image super-resolution via sparse representation," *IEEE trans. image process.*, pp.2861-2873, 2010.
- [22] R. Zeyde, M. Elad, and M. Protter, "On single image scale-up using sparse-representations," *In Curves and Surfaces*, pp.711-730, Springer, 2012.
- [23] C. Dong, C. C. Loy, K. He, and X. Tang, "Learning a deep convolutional network for image super-resolution," *in Proc. 13th Eur. Conf.*

- Comput. Vis.*, pp. 184-199. Springer, 2014.
- [24] C. Dong, C. C. Loy, K. He, and X. Tang, "Image super-resolution using deep convolutional networks," *In TPAMI*, vol. 38, no. 2, pp. 295-307, 2016.
- [25] L. Chen, X. Yang, G. Jeon, M. Anisetti, and K. Liu, "A trusted medical image super-resolution method based on feedback adaptive weighted dense network," *Artificial Intelligence in Medicine*, 2020.
- [26] J. Kim, J. K. Lee, and K. M. Lee, "Accurate image super-resolution using very deep convolutional networks," *in Proc. IEEE Conf. Comput. Vis. Pattern Recognit.*, pp. 1646-1654, 2016.
- [27] Y. Tai, Y. Jian, and X. Liu, "Image super-resolution via deep recursive residual network," *in Proc. IEEE Conf. Comput. Vis. Pattern Recognit.*, pp. 2790-2798, 2017.
- [28] K. He, X. Zhang, S. Ren, and J. Sun, "Deep residual learning for image recognition," *in Proc. IEEE Conf. Comput. Vis. Pattern Recognit.*, pp. 770-778, 2016.
- [29] S. Zagoruyko and N. Komodakis, "Wide residual networks," *in Proc. 27th British Mach. Vis. Conf.*, pp. 1-13, 2016.
- [30] R. Timofte, V. De Smet, and L. Van Gool, "A+: Adjusted anchored neighborhood regression for fast super-resolution," *In Asian Conference on Computer Vision (ACCV)*, pp.111-126, Springer, 2014.
- [31] I. Goodfellow, J. Pouget-Abadie, M. Mirza, B. Xu, and D. Warde-Farley et al., "Generative adversarial nets," *In NIPS*, pp. 2672-2680, 2014.
- [32] X. Wang, K. Y u, C. Dong, X. Tang, and C. C. Loy, "Deep network interpolation for continuous imagery effect transition," *In CVPR*, pp. 1692-1701, 2019.
- [33] X. Wang, K. Y u, S. Wu, J. Gu, and Y. Liu et al., "Esrgan: Enhanced super-resolution generative adversarial networks," *In ECCV*, 2018.
- [34] Y. Zhang, K. Li, K. Li, L. Wang, and B. Zhong et al., "Image super-resolution using very deep residual channel attention networks," *In ECCV*, pp. 286-301, 2018.
- [35] C. Ledig, L. Theis, F. Huszár, J. Caballero, and A. Cunningham et al., "Photo-realistic single image super-resolution using a generative adversarial network," *In CVPR*, vol. 2, no. 3, pp. 4, 2017.
- [36] D. K. Sodickson, W. J. Manning, "Simultaneous acquisition of spatial harmonics (SMASH): fast imaging with radiofrequency coil arrays," *Magn. Reson. Med.*, vol. 38, pp. 591-603, 1997.
- [37] K. P. Pruessmann, M. Weiger, M. B. Scheidegger, P. Boesiger, "SENSE: sensitivity encoding for fast MRI," *Magn. Reson. Med.*, vol. 42, pp. 952-962, 1999.
- [38] M. A. Griswold, P. M. Jakob, R. M. Heidemann, M. Nittka, and V. Jellus, et al., "Generalized autocalibrating partially parallel acquisitions (GRAPPA)," *Magn. Reson. Med.*, vol. 47, pp. 1202-1210, 2002.
- [39] M. Akçakaya, S. Moeller, S. and Weingärtner, "Scan-specific robust artificial-neural-networks for k-space interpolation (RAKI) reconstruction: Database-free deep learning for fast imaging," *Magn. Reson. Med.*, vol. 81, no. 1, pp. 439-453, 2019.
- [40] J. P. Haldar, "Autocalibrated LORAKS for fast constrained MRI reconstruction," *In: Proc. IEEE Int. Symp. Biomed. Imag.*, pp. 910-913, 2015.
- [41] P. J. Shin, P. E. Larson, M. A. Ohliger, M. Elad, and J. M. Pauly et al., "Calibrationless parallel imaging reconstruction based on structured low-rank matrix completion," *Magn. Reson. Med.*, vol. 72, no. 4, pp. 959-970, 2014.
- [42] J. P. Haldar and J. Zhuo, "P-LORAKS: Low-rank modeling of local k-space neighborhoods with parallel imaging data," *Magn. Reson. Med.*, vol. 75, no. 4, pp. 1499-1514, 2016.
- [43] C. Yang, X. Liao, Y. Liao, M. Zhang, and Q. Liu, "Super Resolution of MR via Learning Virtual Parallel Imaging," *In 10th National Annual Meeting of Medical Imaging Physics*, 2021.
- [44] J. W. Carlson, "An algorithm for NMR imaging reconstruction based on multiple RF receiver coils," *J. Magn. Reson.*, vol. 74, pp. 376-380, 1987.
- [45] M. Hutchinson and U. Raff, "Fast MRI data acquisition using multiple detectors," *Magn. Reson. Med.*, vol. 6, pp. 87-91, 1988.
- [46] P. Ullmann, S. Junge, M. Wick, F. Seifert, and W. Ruhm et al., "Experimental analysis of parallel excitation using dedicated coil setups and simultaneous RF transmission on multiple channels," *Magn. Reson. Med.*, vol. 54, pp. 994-1001, 2005.
- [47] U. Fontius, R. Baumgartl, U. Boettcher, G. Doerfler, and F. Hebrank et al., "A flexible 8-channel RF transmit array system for parallel excitation," *In: Proceedings of the 14th Annual Meeting of ISMRM*, 2006.
- [48] C. H. Leussler, J. Stimma, and P. Roßschmann, "The bandpass birdcage resonator modified as a coil array for simultaneous MR acquisition," *In: Proceedings of the 5th Annual Meeting of ISMRM*, 1997.
- [49] P. Vernickel, P. Roschmann, C. Findekklee, K. M. Ludeke, and C. Leussler et al., "Eight-channel transmit/receive body MRI coil at 3T," *Magn. Reson. Med.*, vol. 58, pp. 381-389, 2007.
- [50] J. A. Nordmeyer-Massner, N. De Zanche, and K. P. Pruessmann, "Mechanically adjustable coil array for wrist MRI," *Magn. Reson. Med.*, vol. 61, pp. 429-438, 2009.
- [51] C. Thalhammer, W. Renz, L. Winter, F. Hezel, and J. Rieger et al., "Two-dimensional sixteen channel transmit/receive coil array for cardiac MRI at 7.0 T: design, evaluation, and application," *J. Magn. Reson. Imaging*, vol. 36, pp. 847-857, 2012.
- [52] M. Blaimer, M. Gutberlet, P. Kellman, F. A. Breuer, H. Köstler, and M. A. Griswold, "Virtual coil concept for improved parallel MRI employing conjugate symmetric signals," *Magn. Reson. Med.*, vol. 61, pp. 93-102, 2009.
- [53] M. Blaimer, P. M. Jakob, and F. A. Breuer, "Regularization method for phase-constrained parallel MRI," *Magn. Reson. Med.*, vol. 72, pp. 166-171, 2014.
- [54] C. Liao, M. K. Manhard, and B. Bilgic et al. "Phase-matched virtual coil reconstruction for highly accelerated diffusion echo-planar imaging," *NeuroImage*, vol. 94, pp. 291-302, 2019.
- [55] M. Blaimer, M. Heim, D. Neumann, P.M. Jakob, S. Kannengiesser, F.A. Breuer, "Comparison of phase-constrained parallel MRI approaches: analogies and differences," *Magn. Reson. Med.*, vol. 75, pp. 1086-1099, 2016.
- [56] B. Bilgic, T. H. Kim, C. Liao, M. K. Manhard, and L. L. Wald et al., "Improving Parallel Imaging by Jointly Reconstructing Multi-Contrast Data," *Magn. Reson. Med.*, vol. 80, pp. 619-632, 2018.
- [57] H. F. Wang, S. Jia, and Y. C. Chang et al., "Improving GRAPPA reconstruction using joint nonlinear kernel mapped and phase conjugated virtual coils," *Phys. Med. Biol.*, vol. 64, pp. 1-10, 2019.
- [58] X. Liu, E. S. Hui, H. C. Chang, et al., "Elimination of residual aliasing artifact that resembles brain lesion on multi-oblique diffusion-weighted echo-planar imaging with parallel imaging using virtual coil acquisition," *J. magn. reson. Imaging*, 2019.
- [59] Q. Liu and H. Leung, "Variable augmented neural network for decolorization and multi-exposure fusion," *Inf. Fusion*, vol. 46, pp. 114-127, 2019.
- [60] D. P. Kingma and P. Dhariwal, "Glow: Generative flow with invertible 1x1 convolutions," *In NeurIPS*, pp. 10236-10245, 2018.
- [61] Y. Xing, Z. Qian, and Q. Chen, "Invertible image signal processing," *In CVPR*, 2021.
- [62] M. Xiao, S. Zheng, C. Liu, Y. Wang, D. He, G. Ke, J. Bian, Z. Lin, and T. Liu, "Invertible image rescaling," *In ECCV*, 2020.
- [63] L. Dinh, J. Sohl-Dickstein, and S. Bengio, "Density estimation using Real NVP," *arXiv preprint arXiv:1605.08803*, 2016.
- [64] G. Eilertsen, J. Kronander, G. Denes, R. K. Mantiuk, and J. Unger, "HDR image reconstruction from a single exposure using deep cnns," *ACM transactions on graphics*, vol. 36, no. 6, pp. 1-15, 2017.
- [65] F. Huang, S. Vijayakumar, Y. Li, et al., "A software channel compression technique for faster reconstruction with many channels," *Magn. Reson. Imaging*, vol. 26, no. 1, pp. 133-141, 2008.
- [66] T. Zhang, J. M. Pauly, S. S. Vasanawala, and M. Lustig, "Coil compression for accelerated imaging with Cartesian sampling," *Magn. Reson. Med.*, vol. 69, no. 2, pp. 571-582, 2013.
- [67] R. Roy and T. Kailath, "ESPRIT—estimation of signal parameters via rotational invariance techniques," *IEEE Trans. Acoust.*, vol. 37, pp. 984-995, 1989.
- [68] M. Murphy, K. Keutzer, S. Vasanawala, M. Lustig, "Clinically feasible reconstruction time for 1-SPiRiT parallel imaging and compressed sensing MRI," *In Proceedings of the 18th Annual Meeting of ISMRM*, p. 4854, 2010.